Journal of Power Sources xxx (2017) 1–7

Contents lists available at ScienceDirect

Journal of Power Sources

journal homepage: www.elsevier.com/locate/jpowsour

Effect of cathode thickness on the performance of planar Na-$NiCl_2$ battery

Xiaochuan Lu [a, *], Hee Jung Chang [a], Jeff F. Bonnett [a], Nathan L. Canfield [a], Keeyoung Jung [b], Vincent L. Sprenkle [a], Guosheng Li [a, **]

[a] Electrochemical Materials and Systems Group, Pacific Northwest National Laboratory, Richland, WA 99352, USA
[b] Materials Research Division, Research Institute of Industrial Science & Technology, Pohang, South Korea

HIGHLIGHTS

- Performance of planar Na-$NiCl_2$ cells was primarily limited by the charging current.
- Cells with 1x and 2x cathodes were dominated by ohmic resistance up to 105 mA/cm^2.
- The cell with 3x cathode retained 27% of the capacity at a power output of 200 mW/cm^2.

ARTICLE INFO

Article history:
Received 27 April 2017
Received in revised form
9 June 2017
Accepted 7 July 2017
Available online xxx

Keywords:
Na-beta alumina batteries
Tubular and planar designs
Na-$NiCl_2$ cell
Electrode thickness
Power output

ABSTRACT

Na-beta alumina batteries (NBBs) are one of the most promising technologies for renewable energy storage and grid applications. Commercial NBBs are typically constructed in tubular designs, primarily because of their ease of sealing. However, planar designs are considered superior to tubular counterparts in terms of power output, cell packing, ease of assembly, and thermal management. In this paper, the performance of planar NBBs has been evaluated at an intermediate temperature. In particular, planar Na-$NiCl_2$ cells with different cathode loadings and thicknesses have been studied at 190 °C. The effects of the cathode thickness, charging current, and discharging power output on the cell capacity and resistance have been investigated. More than 60% of theoretical cell capacity was retained with constant discharging power levels of 200, 175, and 100 mW/cm^2 for 1x, 2x, and 3x cathode loadings, respectively. The cell resistance with 1x and 2x cathode loadings was dominated by ohmic resistance with discharging currents up to 105 mA/cm^2, while for 3x cathode loading, it was primarily dominated by ohmic resistance with currents less than 66.67 mA/cm^2 and by polarization resistance above 66.67 mA/cm^2.

© 2017 Elsevier B.V. All rights reserved.

1. Introduction

Electrochemical energy storage devices or rechargeable batteries have attracted increasing attention recently for transportation and grid-scale applications [1,2]. Among various types of technologies, Na-beta alumina batteries (NBBs), based on a β″-Al_2O_3 solid electrolyte (BASE) and a molten sodium anode [1,3,4], have been widely studied due to their high energy density, high efficiency, and good cycle life. Two main types of NBBs have been investigated, categorized by cathode material. One is the sodium-sulfur (Na-S) battery, which uses molten sulfur/polysulfides as the cathode materials [3,4]. The other is the sodium-metal halide (Na-MH or ZEBRA) battery, in which a solid transition metal halide, such as $NiCl_2$ or $FeCl_2$, is typically used as the cathode material [3,5–8].

In both Na-S and Na-MH batteries, the BASE could be either in a planar or tubular shape, depending on the cell design. A cell with a tubular BASE was first reported by Kummer and Weber [9] and the design has been retained by most researchers and industries today. One of the major advantages of the tubular designs is relative ease of sealing between α-Al_2O_3 rings (or holder) and metal parts. The internal diameter of the α-Al_2O_3 rings is typically 20–60 mm with a thickness of 1–2 mm for practical applications [10]. Because the α-Al_2O_3 rings have a much smaller area than the BASE tubes, a relatively small mechanical load can be applied to the α-Al_2O_3 rings during compression or thermocompression sealing. In the planar batteries, however, the diameter of the α-Al_2O_3 rings is at least

* Corresponding author.
** Corresponding author.
E-mail addresses: Xiaochuan.Lu@pnnl.gov (X. Lu), Guosheng.Li@pnnl.gov (G. Li).

http://dx.doi.org/10.1016/j.jpowsour.2017.07.029
0378-7753/© 2017 Elsevier B.V. All rights reserved.

80 mm and the optimum size is ~250 mm to achieve a reasonable energy density for practical applications [4]. Unfortunately, the much larger area of these α-Al_2O_3 rings makes it extremely difficult to perform thermocompression sealing. The α-Al_2O_3 rings typically cannot withstand the large load applied to them during the sealing because of their inherent weakness.

Aside from the abovementioned challenges, planar designs can offer overwhelming advantages in areas such as power output, cell packaging, ease of assembly, and thermal management. For example, cells with planar designs can have larger capacity with a thicker electrode and a small electrolyte area for applications when peak power output is less critical, while cells with a maximum electrolyte area for a given cell volume (i.e., a thinner electrode) may be preferred for applications when the power is limited. Planar designs also simplify interconnection and allow a more compact stacking of single cells, which improves the overall cell packaging efficiency. Cells with the more compact stacking helps to keep cell temperature within an appropriate range, and therefore minimize heat loss during cell idling.

We have been working on advanced planar type Na-MH batteries operated at temperatures below 200 °C. Our recent studies reported a remarkable battery performance with an excellent capacity retention over 1000 cycles [11]. The high energy density and long cycle life were ascribed to a low material degradation rate at the reduced temperature. Lowering operating temperature from 280 to 190 °C also provides opportunities to develop alternative sealing materials including the conventional high temperature polymers, which was studied in our more recent work [12]. The designing and testing of larger planar cells with polymer seals are under investigation and will be reported in the future.

In this work, we investigated the performance of planar Na-MH batteries (e.g., Na-$NiCl_2$ batteries) at an intermediate temperature of 190 °C. In particular, the effects of cathode thickness (or loading), charging current, and discharging power output on the cell capacity and resistance have been thoroughly evaluated. The results reported in this work present a step forward for the practical application of the planar type Na-MH batteries.

2. Experimental

2.1. Fabrication of BASE discs

BASE discs were fabricated using a vapor phase process, as described previously [3,13–15]. Starting powders were high purity α-Al_2O_3 (Almatis, >99.8%) and yttria-stabilized zirconia (YSZ, UCM Advanced Ceramics, 8 wt%). 70 vol% α-Al_2O_3 and 30 vol% YSZ were ball milled with a dispersant (Phospholan PS-236, Akzo Nobel), solvents (methyl ethyl ketone/ethanol), a plasticizer (benzyl butyl phthalate, Aldrich) and a binder (Butvar® B-79) to make slurry. After the slurry was cast into thin sheets (~125 μm), the sheets were laminated and laser-cut to form circular discs. The discs were fired at 1600 °C in air to achieve full density (>99%). The sintered α-Al_2O_3/YSZ discs were then placed in loose β″-Al_2O_3 powder and heat treated at 1450 °C in air to convert α-Al_2O_3 into β″-Al_2O_3. The β″-Al_2O_3 powder used in the conversion process was synthesized using boehmite, Na_2CO_3, and Li_2CO_3 via a solid-state reaction [3,14]. The conversion occurred by a coupled transport of sodium and oxygen ions from the β″-Al_2O_3 powder to the samples. The thickness of the converted composite β″-Al_2O_3/YSZ discs was ~600 μm.

2.2. Cell construction and testing

During cell testing, the cell cathode was granules consisting of Ni, NaCl, and small amounts of additives. After a final drying treatment to eliminate all traces of moisture under vacuum at 200 °C, molten $NaAlCl_4$ secondary electrolyte was infiltrated into the granules. The weights of the cathode granules used in the cells were 1, 2, and 3 g for 1x, 2x, and 3x cathode loading, respectively. A foil and a spring made of Mo were placed on the top of the cathode as a current collector. On the anode side, a spring-loaded metal shim was inserted into the anode compartment as a sodium reservoir. Anode and cathode end plates were then compressed onto the α-Al_2O_3 ring with metal O-rings. Nickel leads were welded to the electrode end plates as current collectors. The active cell area was ~3 cm^2.

The assembled cells were heated in air to 190 °C at which they were initially charged up to 2.8 V with a constant current of 10 mA (i.e., 3.33 mA/cm^2). The cells were then discharged back to a cut-off voltage of 1.8 V at the same current. After the initial cycles, the cells were cycled between the cut-off voltages of 1.8 and 2.8 V. The charge was under constant currents of 6.67, 16.67, and 25 mA/cm^2 and the discharge was under constant power levels of 75–250 mW/cm^2 (current up to 105 mA/cm^2) for regular cycles.

3. Results and discussion

Cross-section images of the single cell cathodes with 1x, 2x, and 3x loadings are shown in Fig. S1. The thicknesses of the cathodes were around 2, 4, and 6 mm, respectively, which was consistent with the cathode loading levels. The initial performance of the cells with the different loadings is shown in Fig. 1a–c. The cell capacities were only 60–80% of the theoretical values during the initial charge, which was likely due to the incomplete wetting of liquid sodium on the surface of the BASE at lower temperatures, as we described previously [16]. During the subsequent cycles, the wetting performance was gradually improved and the cell capacities increased accordingly. The cells with 2x and 3x cathode loadings achieved full capacities during the second cycle while it took the cell with 1x cathode loading almost 5 cycles to get full capacity. It could be related to larger amounts of sodium left in the anode after the initial charge for higher cathode loadings. More sodium maintained in the anode means a better coverage of sodium on the surface of the BASE, and therefore better wetting performance. The capacities of the cells with 1x, 2x, and 3x cathode loadings finally reached 156.1, 312.6, and 468.4 mAh, respectively, which were almost 100% of the theoretical capacities for these cells, as shown in Table 1.

In order to test the rate capability, the cells with different cathode thicknesses were operated at different charging/discharging rates. Fig. 2 shows the cycling performance of the cell with 1x cathode loading at 190 °C. As shown in Fig. 2a and b, the charge/discharge capacities of the cell at a charging current of 6.67 mA/cm^2 and a discharging power level of 75 mW/cm^2 were around 85% of the theoretical value. When the charging current was increased to 16.67 mA/cm^2; refer to red lines in Fig. 2a, the charge overpotential was significantly larger because of the higher current, and the cell voltage reached the cut-off voltage of 2.8 V earlier than at 6.67 mA/cm^2, which led to a lower charge capacity. The discharging power level was kept at 75 mW/cm^2 and the discharging voltage profile was overlapped with that in the previous cycling at a charging current of 6.67 mA/$cm^2$and a discharging power level of 75 mW/cm^2. The charge/discharge capacities were about 80% of the theoretical value. When the discharging power level was further increased to 100 mW/cm^2, the discharge capacity was limited because of the larger discharge overpotential, which caused the discharge capacity to be lower than 80% of the theoretical value. The subsequent charge capacity was reduced accordingly. It can be concluded that ~80% of the theoretical capacity was retained with charging current and discharging power level at or lower than 16.67 mA/cm^2 and 75 mW/cm^2, respectively.

Please cite this article in press as: X. Lu, et al., Journal of Power Sources (2017), http://dx.doi.org/10.1016/j.jpowsour.2017.07.029

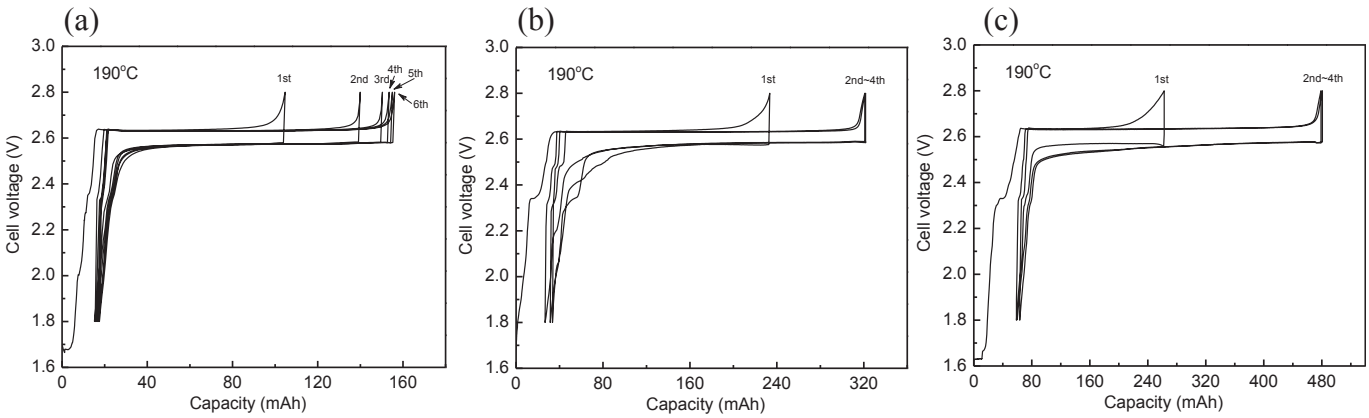

Fig. 1. Single cell performance with (a) 1x, (b) 2x, and (c) 3x cathode loadings at a constant current of 3.33 mA/cm^2 at 190 °C.

Table 1
Cathode thickness and capacity of the single cells with various cathode loading levels.

	Cathode loading		
	1x	2x	3x
Cathode thickness (mm)	~2	~4	~6
Cell capacity (mAh)	156.1	312.6	468.4
Theoretical capacity (mAh)	156.8	313.6	470.4
$\frac{\text{Cell capacity}}{\text{Theoretical capacity}} \times 100\%$	99.6	99.7	99.6

The cell was further tested at a constant charging current of 25 mA/cm^2 and discharging power levels of 100–250 mW/cm^2, as shown in Fig. 3. All of the charge voltage profiles overlapped with each other because they had the same charging current. However, with the increase of the discharging power level, the discharge overpotential increased accordingly and the voltage reached the lower cut-off voltage of 1.8 V earlier, which led to a limited discharge, and therefore a lower capacity. As shown in Fig. 3b, the cell charge/discharge capacities decreased from around 70 to 53% of the theoretical value with the increase of discharging power levels from 100 to 250 mW/cm^2. At a charging current of 25 mA/cm^2, the cell capacity can achieve around 50% of the theoretical value with discharging power level as high as 250 mW/cm^2.

Fig. 3c shows the cell discharging voltages and currents at different discharging power levels at 30, 50, and 70% state of charges (SOCs), as marked with vertical lines in Fig. 3a. Overall, the cell voltage showed an excellent linear relationship with the current particularly at 50 and 70% SOCs. In a fuel cell or battery, the output or discharging voltage, V_{out}, can be expressed as [17].

$$V_{out} = OCV - \eta_a - \eta_c - iR$$

η_a and η_c are polarizations in the anode and cathode. R is the ohmic resistance from the electrolyte and electrodes. The excellent linear relationship between V_{out} and i observed in Fig. 3c indicated that the overall cell resistance was dominated by the ohmic resistance, including contributions from both the electrolyte and electrodes. The polarization resistances were negligible compared to the ohmic resistance in the current cell design with 1x cathode loading and the discharging currents up to 100 mA/cm^2. Based on the fitting results in Fig. 3c, the area specific resistances (ASRs) were 4.35, 4.29, and 7.53 Ω cm^2 in the start, middle, and end of discharge (e.g., 70, 50, and 30% SOCs, refer to Fig. 3a). The higher resistance at the end of discharge could be related to an insufficient amount of sodium on the anode side, which might not be able to cover the full active area of the BASE, and therefore lead to a higher cell resistance.

Fig. 3d shows the cell capacities at different charging currents

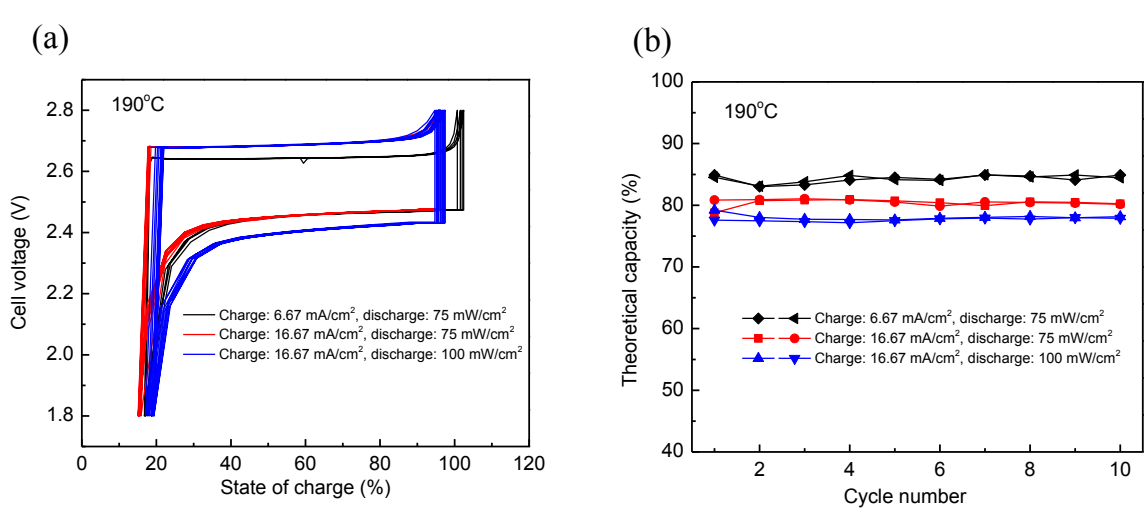

Fig. 2. Cycling performance of the cell with 1x cathode loading at constant charging currents of 6.67 and 16.67 mA/cm^2 at 190 °C: (a) cell voltage profiles during 10 cycles and (b) charge/discharge capacities during 10 cycles.

Please cite this article in press as: X. Lu, et al., Journal of Power Sources (2017), http://dx.doi.org/10.1016/j.jpowsour.2017.07.029

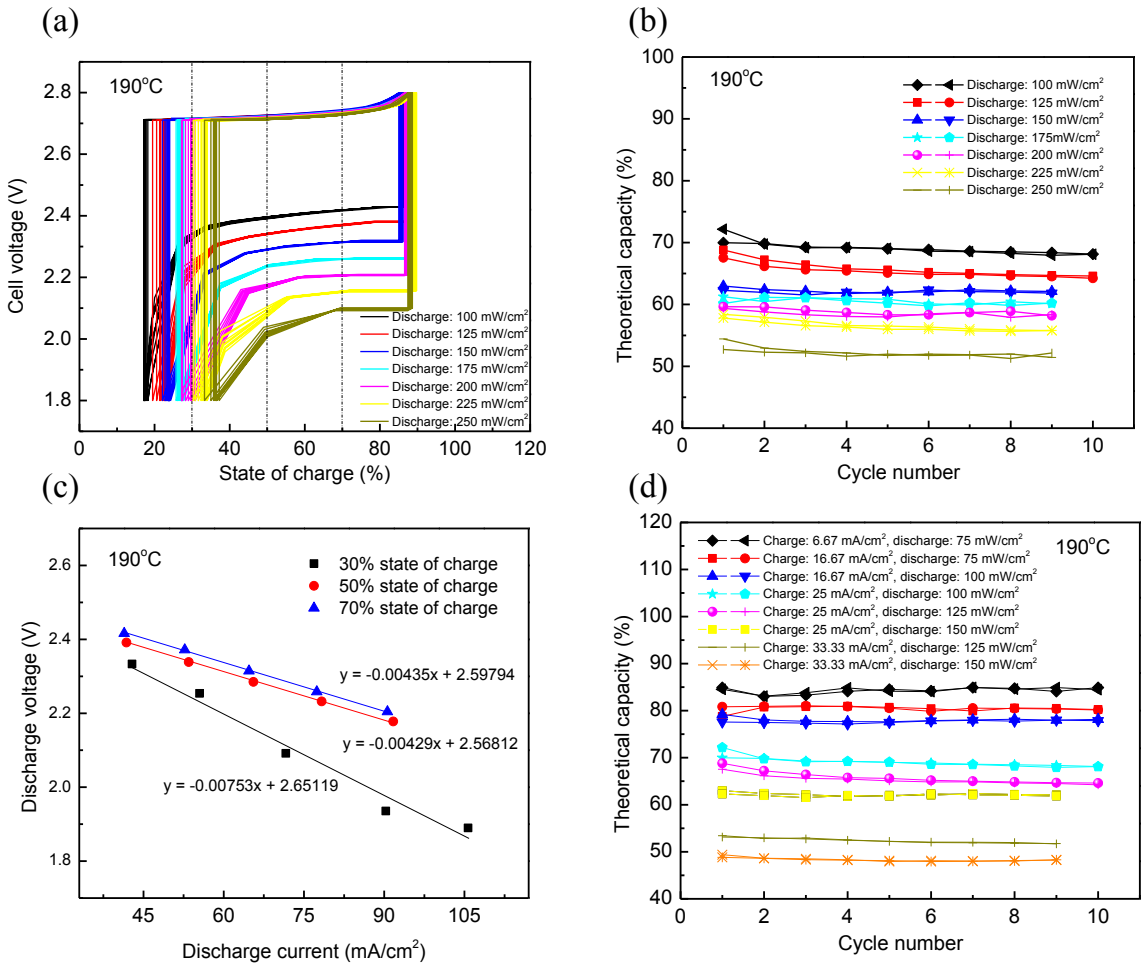

Fig. 3. Cycling performance of the cell with 1x cathode loading at constant charging current of 25 mA/cm^2 at 190 °C: (a) cell voltage profiles during 10 cycles, (b) charge/discharge capacities during 10 cycles, (c) discharging voltages and currents at the different SOCs (marked in Fig. 3a), and (d) charge/discharge capacities compared with those at lower currents.

and discharging power levels for the cell with 1x cathode loading. With the charging current and discharging power level up to 16.7 mA/cm^2 and 100 mW/cm^2, the cell capacities were above 80% of the theoretical value. When the current was increased to 25 mA/cm^2, the cell capacities decreased to around 65% of theoretical capacity. With further increase of the charging current to 33.33 mA/cm^2, the cell capacities quickly dropped to around 50% of the theoretical capacity. It can be concluded that the charge/discharge capacities were primarily limited by the charging current for 1x cathode loading.

Fig. 4 shows the cycling performance of the cell with 2x cathode loading at 190 °C. As shown in Fig. 4a and b, the charge/discharge capacities of the cell at a charging current of 6.67 mA/cm^2 and a discharge power level of 75 mW/cm^2 were slightly lower than 80% of the theoretical capacity. With the charging current and discharging power level increased to 16.67 mA/cm^2 and 100 mW/cm^2, the cell capacities dropped to around 75% of the theoretical value. Compared to the cell performance with 1x cathode loading (refer to Fig. 2b), it can be seen that, with discharging currents and power levels at or below 16.67 mA/cm^2 and 75 mW/cm^2, the cell performance was not significantly affected by the increase of cathode thickness from ~2 mm (1x cathode loading) to ~4 mm (2x cathode loading).

Similarly to the cells with 1x cathode loading, the cell with 2x cathode loading was also tested at a constant charging current of 25 mA/cm^2 and different discharging power levels, as shown in Fig. 4c. The cell charge/discharge capacities decreased from around 70 to 55% of the theoretical value with the increase of discharging power levels from 300 to 600 mW. As a comparison, the capacities decreased from around 70 to 60% of the theoretical value under similar conditions for cell with 1x cathode loading (see Fig. 3b). The ASRs were 4.23, 4.29, and 5.71 Ω cm^2 in the start, middle, and end of discharge (e.g., 70, 50, and 30% SOCs) for the cell with 2x cathode loading, as shown in Fig. 4d. These values are very close to those for 1x cathode loading. The cell performance was essentially unaffected by the increase of cell cathode thickness from ~2 to ~4 mm under the current testing conditions. It also should be noted that the ASR of 5.71 Ω cm^2 at the end of discharge for the 2x cathode loading was significantly lower than that for the 1x cathode loading (see Fig. 3c), which was likely due to a larger amount of sodium left at the end of discharge, better coverage of the BASE surface by the liquid sodium, and therefore lower resistance for the cell with 2x cathode loading.

Fig. 5 shows the performance of the cell with 2x cathode loading at different charging currents and discharging power levels. The cell capacities were 80–75% of the theoretical value at charging currents and discharging power levels up to 16.7 mA/cm^2 and 100 mW/cm^2. The capacities dropped to around 65% of the theoretical value when the charging current was increased to 25 mA/cm^2. They were around 55% at a current of 33.33 mA/cm^2. Clearly,

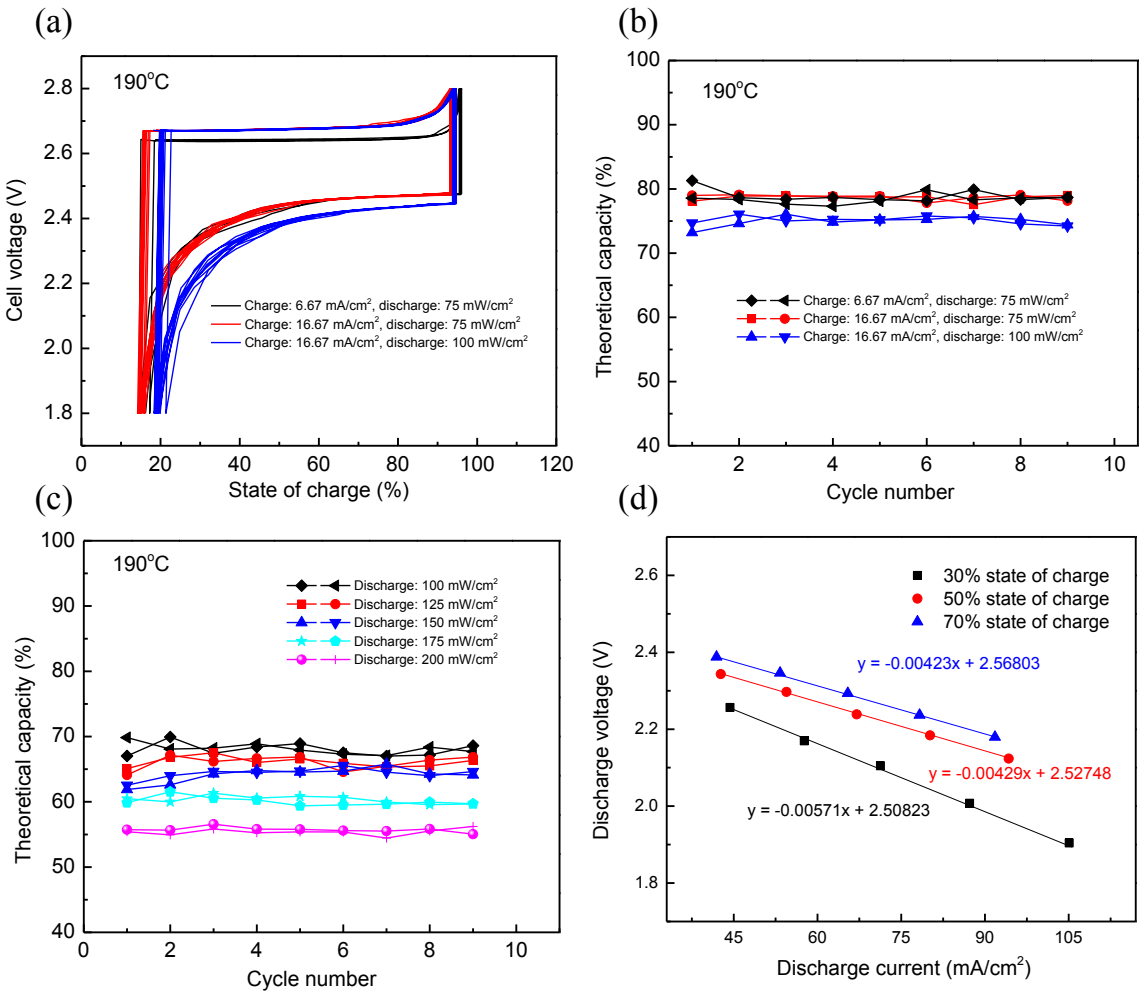

Fig. 4. Cycling performance of the cell with 2x cathode loading at 190 °C: (a) cell voltage profiles (b) charge/discharge capacities at constant charging currents of 6.67 and 16.67 mA/cm^2, (c) charge/discharge capacities at a constant charging current of 25 mA/cm^2, and (d) discharging voltages and currents at different SOCs.

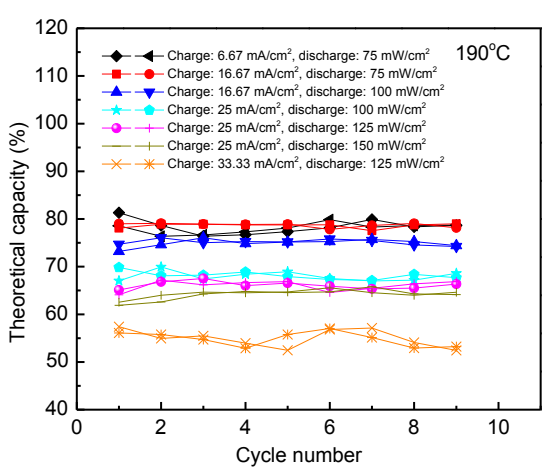

Fig. 5. Charge/discharge capacities of the cell with 2x cathode loading at different charging currents and discharging power levels at 190 °C.

the charge/discharge capacities were limited by the charging current, which was similar to the cell with 1x cathode loading.

Performance of the cell with 3x cathode loading is shown in Figs. 6 and 7. As shown in Fig. 6a and b, with charging currents and discharging power levels at or lower than 16.67 mA/cm^2 and 100 mW/cm^2, the cell charge/discharge capacities were above 75% of the theoretical value. With the charging current increased to 25 mA/cm^2 (refer to Fig. 6c), the capacities decreased from around 60 to less than 30% of the theoretical value with the increase of discharging power levels from 100 to 200 mW/cm^2. Significant decrease in the capacity was observed for the cells with 3x cathode loading compared to those with 1x and 2x cathode loadings (see Figs. 3b and 4c). For example, the capacity decreased from around 70 to 60% of the theoretical value for the cell with 1x cathode and around 70 to 55% of the theoretical value for the cell with 2x cathode under similar conditions. Apparently, the more dramatic decrease in the cell capacity for the 3x cathode was related to the thicker cathode. A thicker cathode means a longer distance for charge transfer, and therefore a higher polarization resistance and inferior cell performance. The cell discharging voltages and currents at different discharging power levels at 30, 50, and 70% SOCs is shown in Fig. 6d. It should be noted that, at high discharging currents (e.g., 77.63 mA/cm^2 or above) and therefore high discharging power levels, the capacity window was narrowed to less than 40% of the theoretical value. The 30% SOC was outside the capacity window, and therefore the voltage and current data was unavailable. However, it was available for the 50 and 70% SOCs since they were in the middle and start of discharge. As shown in Fig. 6d, the linear relationship between V_{out} and i was not as good as for the

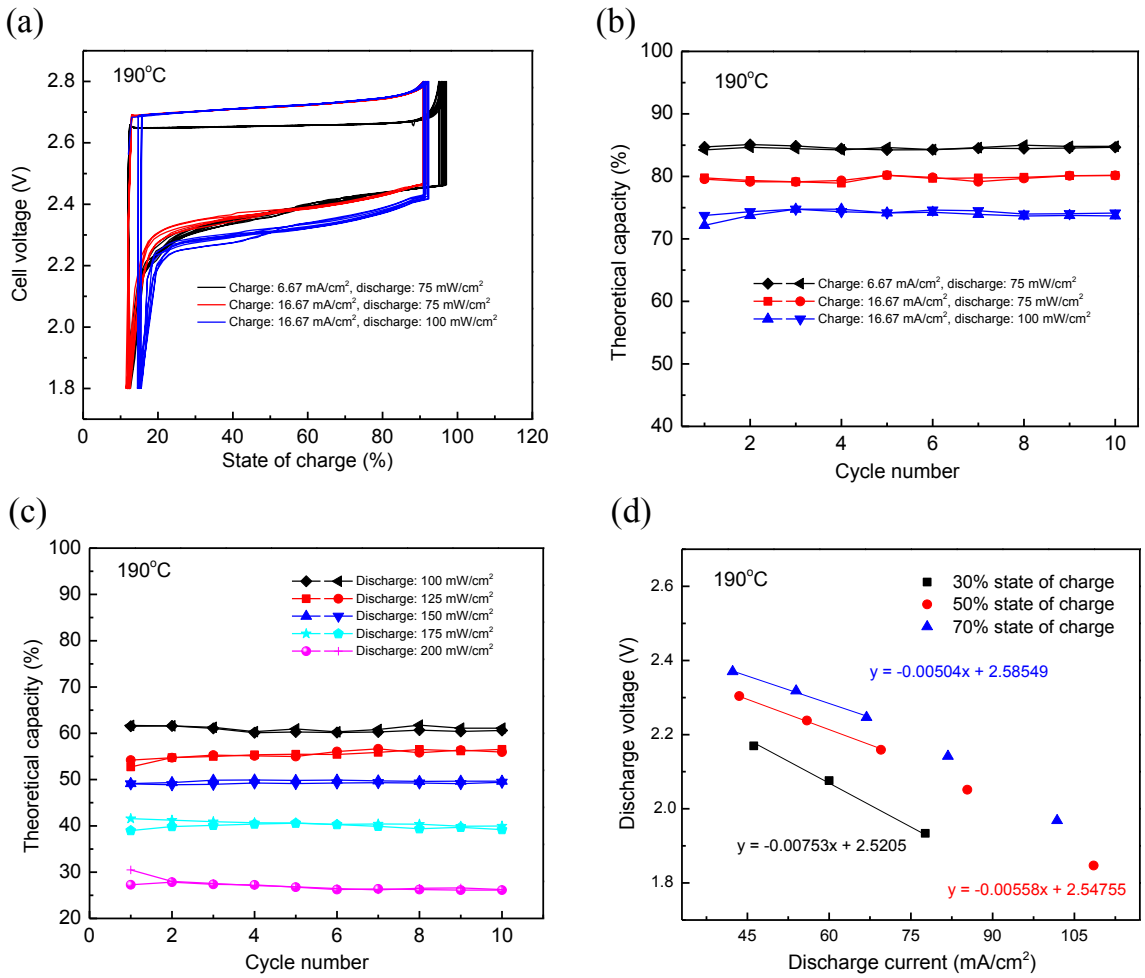

Fig. 6. Cycling performance of the cell with 3x cathode loading at 190 °C: (a) cell voltage profiles (b) charge/discharge capacities at constant charging currents of 6.67 and 16.67 mA/cm^2, (c) charge/discharge capacities at a constant charging current of 25 mA/cm^2, (d) discharging voltages and currents at different SOCs.

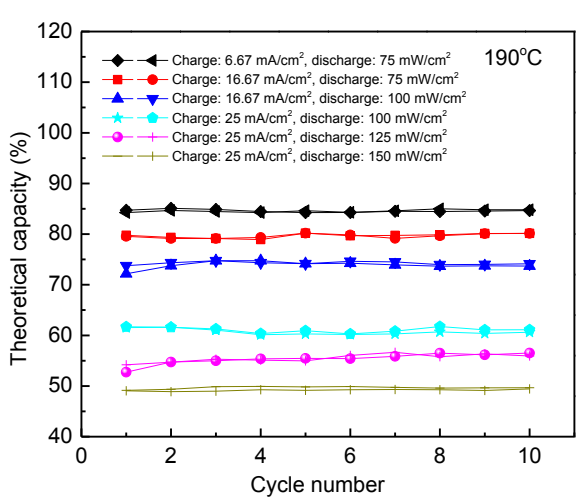

Fig. 7. Charge/discharge capacities of the cell with 3x cathode loading at different charging currents and discharging power levels at 190 °C.

cells with 1x and 2x cathode loadings (see Figs. 3c and 4d), particularly at the currents above 66.67 mA/cm^2 (refer to the red dots for 50% SOC). This suggested that the cell resistance, particularly at the higher current, was dominated by the polarization resistance, which was consistent with the dramatic decrease in the cell capacity as we discussed above. After comparing the cell resistance with different cathode loadings, we can conclude that the resistance with 1x and 2x cathode loadings was dominated by the ohmic resistance with currents up to 105 mA/cm^2. For 3x cathode loading, it was primarily dominated by the ohmic resistance with currents less than 66.67 mA/cm^{2}and by the polarization resistance above 66.67 mA/cm^2.

Fig. 7 compares the charge and discharge capacities for the cell with 3x cathode loading at different charging currents and discharging power levels. The cell capacities were above 70% of the theoretical value at charging currents and discharging power levels up to 16.67 mA/cm^2 and 100 mW/cm^2. The capacities were 60% or less of the theoretical value when the charging current was increased to 25 mA/cm^2. These trends are similar to those cells with 1x and 2x cathode loadings, indicating that the cell capacity is generally controlled by the charging current in the current cell design.

The performance of the single cells with different cathode loadings is compared in Fig. 8. In general, the capacities decreased with the increase of discharging power levels for all of the cells. However, significant decrease in the capacities was observed for the cell with 3x cathode loading, particularly at higher discharging power levels and currents, which is consistent with the results

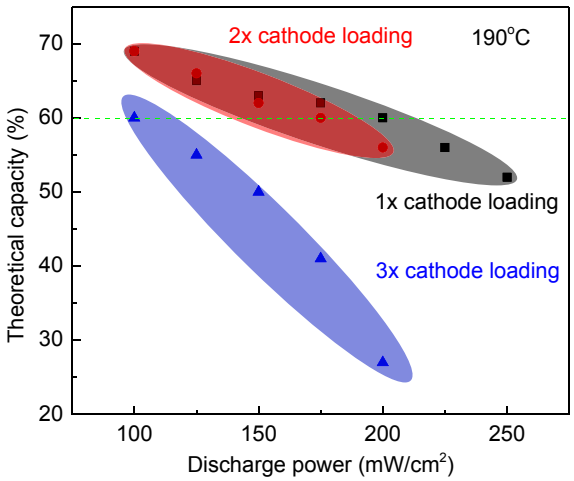

Fig. 8. Comparison of cell capacities at a constant charging current of 25 mA/cm^2 and various discharging power levels at 190 °C.

Table 2
Performance of the single cell with 3x cathode loading at different discharging power levels.

	Discharging Power level (mW/cm^2)				
	100	125	150	175	200
Discharging current density (mA/cm^2)	~40	~60	~70	~80	~100
Discharge rate (C)	~0.4	~0.7	~0.9	~1.3	~2.4
Cell capacity (mAh)	280.8	257.4	234.0	191.9	126.4
$\frac{\text{Cell capacity}}{\text{Theoretical capacity}} \times 100\%$	60	55	50	41	27

above. From Fig. 8, the discharging power levels can be up to 200 mW/cm^2 (~100 mA/cm^2), 175 mW/cm^2 (~80 mA/cm^2), and 100 mW/cm^2 (~40 mA/cm^2) for 1x, 2x, and 3x cathodes to reach a cell capacity of at least 60% of the theoretical value. The performance of the cell with 3x cathode loading was particularly interesting. For example, even with a discharging power level of 200 mW/cm^2 (~100 mA/cm^2 and a rate of ~2.4C), the cell still had a capacity of 27% of the theoretical value (refer to Fig. 8), which indicates this battery is suitable for pulse power applications. The thickness of the cathode (i.e., ~6 mm) in the current design was very close to those in the practical cells. Such high performance at 190 °C indicates this type of planar Na-MH battery is very promising for practical applications compared to the existing high-temperature Na-MH technologies. The detailed performance of the cell with the 3x cathode loading is listed in Table 2.

4. Conclusion

Planar Na-$NiCl_2$ cells with various cathode loading levels and thicknesses have been studied and evaluated at 190 °C. For various cathode loadings, the cell performance (e.g., charge/discharge capacities) was primarily limited by the charging current. With a constant charging current of 25 mA/cm^2, ~60% of the theoretical capacity can be retained with constant discharging power levels of 200, 175, and 100 mW/cm^2 for 1x (~2 mm thick), 2x (~4 mm thick), and 3x (~6 mm thick) cathodes, respectively. The lower capacity for the cell with the 3x cathode loading was related to its greater thickness. The thicker the cathode, the longer the distance required for charge transfer, and therefore higher polarization resistance and inferior cell performance. The cell resistance with 1x and 2x cathode loadings was dominated by ohmic resistance with the discharging currents up to 105 mA/cm^2. For 3x cathode loading, it was primarily dominated by ohmic resistance with the currents less than 66.7 mA/cm^2 and by polarization resistance above 66.7 mA/cm^2. The cell with 3x cathode loading retained 27% of the theoretical capacity even with a discharge power level as high as 200 mW/cm^2 (~100 mA/cm^2 and a rate of ~2.4C). The extraordinary performance of the planar Na-MH battery in the current study suggests it potentially can replace the state-of-the-art high-temperature Na-MH technologies for efficient energy storage.

Acknowledgements

The work is supported by the U.S. Department of Energy (DOE)'s Office of Electricity Delivery & Energy Reliability's storage program (Contract No. 57558) and the International Collaborative Energy Technology R&D Program of the Korea Institute of Energy Technology Evaluation and Planning (KETEP), the Ministry of Trade, Industry and Energy of the Republic of Korea (No. 20158510050010) and POSCO. Pacific Northwest National Laboratory is a multiprogram laboratory operated by Battelle Memorial Institute for the DOE under Contract DE-AC05-76RL01830.

Appendix A. Supplementary data

Supplementary data related to this article can be found at http://dx.doi.org/10.1016/j.jpowsour.2017.07.029.

References

[1] Z. Yang, J. Zhang, M.C.W. Kintner-Meyer, X. Lu, D. Choi, J.P. Lemmon, J. Liu, Chem. Rev. 111 (2011) 3577.
[2] B. Scrosati, J. Grache, J. Power Sources 195 (2010) 2419.
[3] X. Lu, G. Xia, J.P. Lemmon, Z. Yang, J. Power Sources 195 (2010) 2431.
[4] J.L. Sudworth, A.R. Tilley, The Sodium Sulphur Battery, Chapman & Hall, London, 1985.
[5] R.C. Galloway, J. Electrochem. Soc. 134 (1987) 256.
[6] R.J. Bones, D.A. Teagle, S.D. Brooker, F.L. Cullen, J. Electrochem. Soc. 136 (1989) 1274.
[7] R.J. Bones, J. Coetzer, R.C. Galloway, D.A. Teagle, J. Electrochem. Soc. 134 (1987) 2379.
[8] G. Li, X. Lu, J.Y. Kim, V.V. Viswanathan, K.D. Meinhardt, M.H. Engelhard, V.L. Sprenkle, Adv. Energy Mater. 5 (2015) 1500357.
[9] J.T. Kummer, N. Weber, U.S. Patent 3,413,150 (1968).
[10] http://www.ionotec.com/pdfs/NaKbetaceramics.pdf.
[11] G. Li, X. Lu, J.Y. Kim, K.D. Meinhardt, H.J. Chang, N.L. Canfield, V.L. Sprenkle, Nat. Comm. 7 (2016) 10683.
[12] H.J. Chang, X. Lu, J.F. Bonnett, N.L. Canfield, S. Son, Y.C. Park, K. Jung, V.L. Sprenkle, G. Li, J. Power Sources 348 (2017) 150.
[13] X. Lu, G.W. Coffey, K.D. Meinhardt, V.L. Sprenkle, Z. Yang, J.P. Lemmon, ECS Trans. 28 (2010) 7.
[14] X. Lu, J.P. Lemmon, V.L. Sprenkle, Z. Yang, JOM. J. Minerals, Metals Mater. Soc. 62 (2010) 31.
[15] X. Lu, G. Li, J.Y. Kim, D. Mei, J.P. Lemmon, V.L. Sprenkle, J. Liu, Nat. Commun. 5 (2014) 4578.
[16] X. Lu, G. Li, J.Y. Kim, J.P. Lemmon, V.L. Sprenkle, Z. Yang, J. Power Sources 215 (2012) 288.
[17] F. Zhao, A.V. Virkar, J. Power Sources 141 (2005) 79.